Bulletin of the Seismological Society of America, Vol. 105, No. 6, pp. 3050–3067, December 2015, doi: 10.1785/0120140322

Broadband Strong Ground Motion Simulations of Large Subduction Earthquakes

by A. A. Skarlatoudis, P. G. Somerville, H. K. Thio, and J. R. Bayless

Abstract The great subduction earthquakes that occurred recently in Peru, Chile, and Japan have provided unprecedented information about the ground motions generated by such earthquakes. The 23 June 2001 **M** 8.4 Peru earthquake was recorded at eight strong-motion stations; the 27 February 2010 **M** 8.8 Maule, Chile, earthquake was recorded at over 10 strong-motion stations; and the 11 March 2011 **M** 9.0 Tohoku, Japan, earthquake was recorded at more than a thousand stations and produced the most extensive dataset of recordings for any earthquake. For the first time, data are available to guide the generation of ground-motion simulations from great subduction earthquakes. Broadband ground-motion simulations can enhance the usefulness of the recordings of these earthquakes by providing a means of interpolating and extrapolating the recorded data. Once they have been validated, broadband ground-motion simulations can be used for forward predictions of the ground motions of great subduction events in regions such as Cascadia, in which there are no strong-motion recordings of large subduction earthquakes.

In this study, we test our ability to use a hybrid method to simulate broadband strong-motion recordings of megathrust earthquakes by demonstrating that our simulations reproduce the amplitudes of the recorded ground motions without systematic bias. We use simulations to study the distribution of various intensity measures of ground motion caused by these earthquakes and to validate our ground-motion simulation method by comparing the simulated ground motions with recorded ground motions as well as with empirical ground-motion prediction models.

Introduction

Ground motions from great subduction earthquakes make a large contribution to ground-motion hazards in areas located in the vicinity of large subduction zones. In the U.S. probabilistic seismic-hazard maps, the subduction source in the Pacific Northwest region is modeled by earthquakes having magnitudes as large as **M** 9.2. Because these magnitudes are larger than any of the earthquakes on which the most recent empirical ground-motion models (e.g., Atkinson and Boore, 2003; Zhao *et al.*, 2006; Abrahamson *et al.*, 2015) are based, it is important to use all the available information from these recent earthquakes to provide insight into the nature of ground motions from such large events.

The recent occurrence of great subduction earthquakes in Peru, Chile, and Japan provides the first glimpse at what the ground motions from such large earthquakes may be like. The 23 June 2001 **M** 8.4, Arequipa, Peru earthquake (Somerville *et al.*, 2008) was recorded at eight strong-motion stations; the 27 February 2010 **M** 8.8 Maule, Chile, earthquake (Somerville *et al.*, 2013a) was recorded at over 10 strong-motion stations; whereas the 11 March 2011 **M** 9.0 Tohoku earthquake (Somerville *et al.*, 2013b) produced the most extensive dataset of recordings for any earthquake, with more than 1000 recordings from each of K-NET and KiK-Net networks operated by the National Research Institute for Earth Science and Disaster Prevention (NIED) of Japan. For the first time, data are available to guide the generation of ground-motion scenarios from great subduction earthquakes. Broadband ground-motion simulations can enhance the usefulness of the recordings of these earthquakes by providing a means of interpolating and extrapolating the recorded data.

The broadband ground-motion simulation method used in this study is based on the work of Somerville *et al.* (1991), Somerville (1993), and Graves and Pitarka (2004, 2010). It is a hybrid technique that computes the long- and short-period ranges separately and then combines the two to produce a single time history using appropriate matched filters. At periods longer than 3 s, the methodology is deterministic and contains a theoretically rigorous representation of fault rupture and wave propagation effects. At periods shorter than 3 s, it uses an empirical representation of source radiation and scattering derived from the recordings of a smaller earthquake, which is combined with a simplified theoretical representation of wave propagation. The method is relatively simple to apply because the only earthquake-specific parameters needed as input are

seismic moment, fault dimensions and geometry, hypocenter location, and a generalized model of the slip distribution. All other source parameters are determined using the scaling relations described in the following sections. Recently, the method has been applied for the first time for the simulation of the ground motions of an intraslab earthquake that occurred in California (2010 **M** 6.5 Ferndale earthquake). It reproduced the basic characteristics of the ground motions of this earthquake without systematic bias (Pitarka *et al.*, 2013).

As described in detail below, we demonstrate the capability to simulate broadband ground motions from great subduction earthquakes and validate that capability by demonstrating that it reproduces the amplitudes of the recorded ground motions of large earthquakes without systematic bias.

Earthquake Source Scaling Relations of Subduction Earthquakes

Somerville *et al.* (2002) developed scaling relations for the source parameters of subduction earthquakes based on the rupture models of seven large earthquakes. These models are analogous to those developed for crustal earthquakes (Somerville *et al.*, 1999). The subduction earthquakes used in these scaling relations include three earthquakes for which we have derived rupture models: 1923 Tokyo, Japan (Wald and Somerville, 1995); 1944 Tonankai, Japan (Ichinose *et al.*, 2003); and 2001 Peru (Somerville *et al.*, 2003). The rupture models portray the spatial and temporal distribution of slip on the fault plane, as inferred from strong-motion recordings, teleseismic data, and in some cases geodetic and tsunami observations. The scaling relations describe the scaling with seismic moment of rupture area, rise time, asperity dimensions, and the corner periods of spatial wavenumber models of fault-slip heterogeneity, which control the spatial distribution of slip and slip velocity. Later studies by Murotani *et al.* (2008, 2013) using a larger dataset give smaller rupture areas and larger average displacements than do those of Somerville *et al.* (2002).

For our ground-motion simulations, we need a relationship between seismic moment and rise time. Murotani *et al.* (2008, 2013) did not develop such a relationship, so we used the one developed by Somerville *et al.* (2002) based on the maximum slip velocity (Ishii *et al.*, 2000). They found the rise time for subduction earthquakes is given by

$$T_r = 1.8 \times 10^{-9} \times M_0^{1/3}. \quad (1)$$

Procedure for Broadband Strong Ground Motion Simulation

We used a hybrid broadband ground-motion simulation approach, based on frequency–wavenumber Green's functions for long periods (>3 s) and on a semistochastic ray theory method (Somerville *et al.*, 1991) for shorter periods, to simulate broadband ground motions for large subduction earthquakes. We show the simulation procedure successfully reproduces the recorded ground motions of the earthquakes in Arequipa, Peru (Somerville *et al.*, 2008), Maule, Chile (Somerville *et al.*, 2013a), and Tohoku, Japan (Somerville *et al.*, 2013b).

Specifically, we used the Caleta de Campos rock-site recording of an aftershock of the 1985 Michoacan, Mexico, earthquake (described in detail by Cohee *et al.*, 1991) as an empirical source function in our simulations. Additional information about the empirical source function and how it is used can be found in Somerville *et al.* (1991).

In the hybrid broadband simulation procedure, the low-frequency and high-frequency components of the ground motions are computed separately and then combined using matched filters. The low-frequency simulation methodology, applied for periods longer than 3.0 s, uses a deterministic representation of source and wave propagation effects (Graves and Pitarka, 2004, 2010) that is based on the approach described by Hartzell and Heaton (1983). The basic calculation is carried out using a 1D frequency–wavenumber integration algorithm.

The earthquake source is specified by a kinematic description of fault rupture, incorporating spatial heterogeneity in slip, rupture velocity, and rise time. Following Hartzell and Heaton (1983), the fault is divided into a number of subfaults. The slip and rise time are constant across each individual subfault, although these parameters are allowed to vary from subfault to subfault. We use a slip velocity function that is constructed using two triangles as shown in Figure 1. This functional form is based on results of dynamic-rupture simulations (e.g., Guatteri *et al.*, 2003). We constrain the parameters of this function as follows:

$$T_r = 1.79 \times 10^{-9} \times M_0^{-1/3},$$
$$T_p = 0.2 \times T_r, \quad \text{and} \quad h = 0.2 \times A, \quad (2)$$

in which M_0 is the seismic moment, T_r is the rise time, and A is normalized to give the desired final slip. The expression for T_r comes from the empirical analysis of Somerville *et al.* (2002). The rupture initiation time (T_i) is determined using the expression

$$T_i = \frac{R}{V_r} - \delta t, \quad (3)$$

in which R is the rupture path length from the hypocenter to a given point on the fault surface; V_r is the rupture velocity and is set at 80% of the local shear-wave velocity (V_S); and δt is a timing perturbation that scales linearly with slip amplitude such that $\delta t = \delta t_0$, in which the slip is at its maximum, and $\delta t = 0$, in which the slip is at the average slip value. For these calculations, we set $\delta t = 0.1$ s. This scaling results in faster rupture across portions of the fault having large slip, as suggested by source inversions of past earthquakes (Hisada, 2001).

The high-frequency simulation methodology, used for periods shorter than 3.0 s, is a semistochastic approach that sums the response for each subfault using empirical source functions. The simulation procedure was originally developed by Somerville *et al.* (1991) following the concepts of Irikura (1978) and Hartzell (1978).

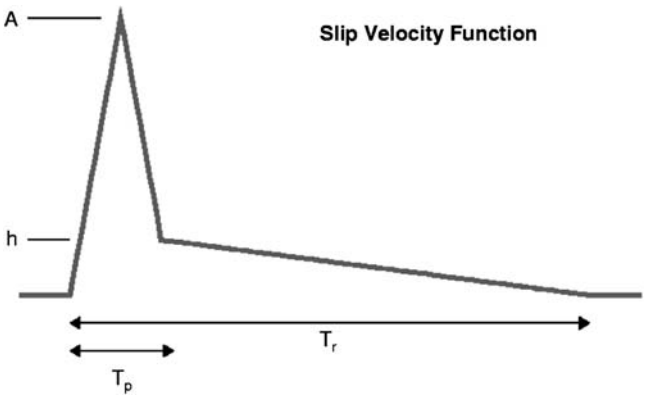

Figure 1. Slip velocity function used in the deterministic simulations (see equation 1).

Case Studies

We studied three large subduction earthquakes that occurred in the past 15 years. The **M** 8.4 Arequipa, Peru, the **M** 8.8 Maule, Chile, and the **M** 9.0 Tohoku, Japan, earthquakes produced large datasets of strong-motion recordings, and the source parameters of these earthquakes are listed in Table 1. In the following sections, the slip models and the crustal structure models that were used for producing the ground-motion simulations for each earthquake are described. Information on the available strong-motion recordings that were used in the validation of the results is also discussed.

23 June 2001 **M** 8.4 Arequipa, Peru, Earthquake

Slip Model. The rupture model of this earthquake was derived by Somerville *et al.* (2003) and is shown in Figure 2a. The rupture zone of the earthquake was ~400 km long, and most of the slip occurred in two asperities, one at shallow depths (5–15 km) and the other at greater depths (25–40 km). The original rupture model was modified for the rupture times using the dependency of rupture velocity on slip described in the preceding section and interpolated at one-quarter the sampling interval of the original slip model. The rupture model (shown in Fig. 2b) is the one that was used for broadband simulations.

Strong-Motion Records. Strong-motion recordings of the Peru earthquake were obtained in Moquegua, Peru, and at seven stations in northern Chile (Boroschek and Comte, 2004), including three in Arica, the locations of which are shown in Figure 2a.

Crustal Structure Model. As described in Somerville *et al.* (2008), the crustal structure model used in the simulations has a surface shear-wave velocity of 1.5 km/s, corresponding to the boundary between National Earthquake Hazards Reduction Program (NEHRP) site categories A and B. To adjust the resulting simulations to lower surface-shear-wave velocities, we used the NEHRP amplitude and period-dependent amplification factors (Building Seismic Safety Council [BSSC], 2003) to scale the response spectra. Ground-motion maps were generated for the B/C category. The B/C category has a surface shear-wave velocity V_{S30} of 760 m/s to represent stiff soil/soft rock-site conditions (the boundary between NEHRP B and C categories).

27 February 2010 **M** 8.8 Maule, Chile, Earthquake

Slip Model. The earthquake rupture model of Lorito *et al.* (2011) was used to simulate the ground motions of the Maule earthquake. This rupture model (shown in Fig. 3a) was derived from both tsunami and geodetic data. The rupture zone of the earthquake was ~625-km-long along strike and 200-km-wide down-dip, and most of the slip occurred in two asperities, adjacent to the earthquake hypocenter at a depth ~35 km. Figure 3b shows the final rupture model used for broadband simulations. The original rupture model from Lorito *et al.* (2011) was modified to take account of variable rupture times (as for the Arequipa slip model) and was interpolated at one-third the sampling interval of the original slip model.

Strong-Motion Records. Strong-motion recordings of the Maule earthquake were obtained at 21 stations, the locations of which are shown in Figure 3 (information from Boroschek and Contreras, 2012). Because of the high-pass filter applied to the recordings (f_{cut} = 0.25 Hz–4 s) during processing, the comparisons with the simulated waveforms were performed for the 0.1–4 s period range.

Crustal Structure Model. The crustal velocity model that was used (listed in Table 2) was derived from the results of Ocola *et al.* (1995). This model was modified to include a shallow layer of low seismic velocity representing weathered rock. This model has a median V_{S30} (average shear-wave velocity for the upper 30 m) of 434 m/s, and consequently all comparisons between the recordings and the synthetic waveforms are presented for sites with this V_{S30}. Whenever it was necessary to adjust the simulations for the median V_{S30} to another surface shear-wave velocity, the NEHRP amplitude and

Table 1
Earthquake Information and Fault Models Adopted

Name	Date (yyyy/mm/dd)	Origin Time (UTC, hh:mm:ss)	Latitude (°)	Longitude (°)	Depth (km)	**M***	Strike (°)	Dip (°)
Arequipa, Peru	2001/06/23	20:33:14	−16.140	−73.312	33	8.3	263	6
Maule, Chile	2010/02/27	06:34:14	−36.120	−72.900	35	8.8	9	12
Tohoku, Japan	2011/03/14	05:46:24	38.297	142.372	30	9.0	193	10

*__M__, moment magnitude.

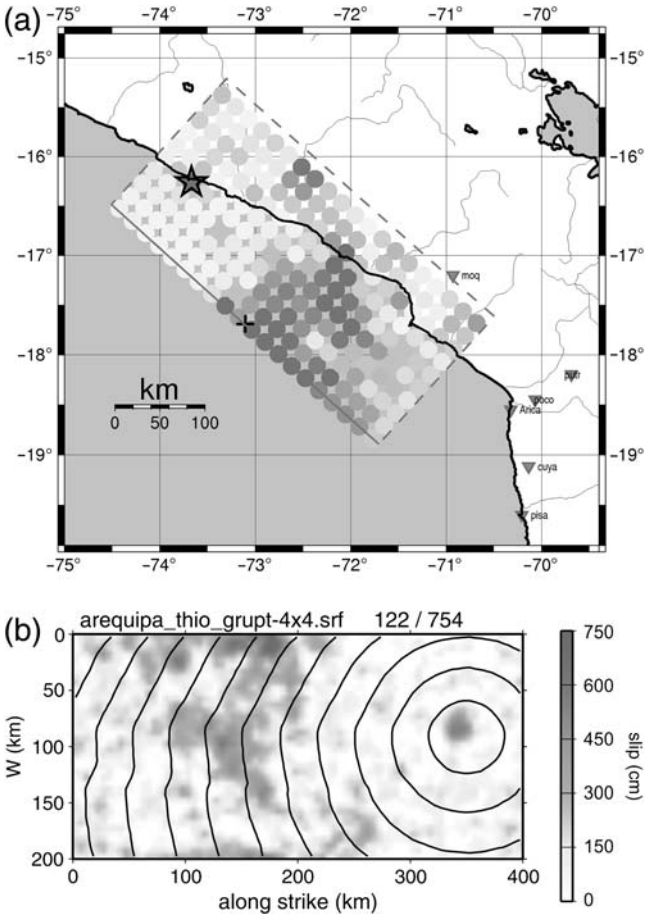

Figure 2. (a) Rupture model of the 2001 **M** 8.4 Arequipa, Peru, earthquake, locations of strong ground motion recording stations, and grid of stations used for the simulations. (b) Resampled rupture model used in the calculations. Slip values (in centimeters) indicated by gray shading. Contours of rupture initiation times across the fault plane are shown at 5 s intervals.

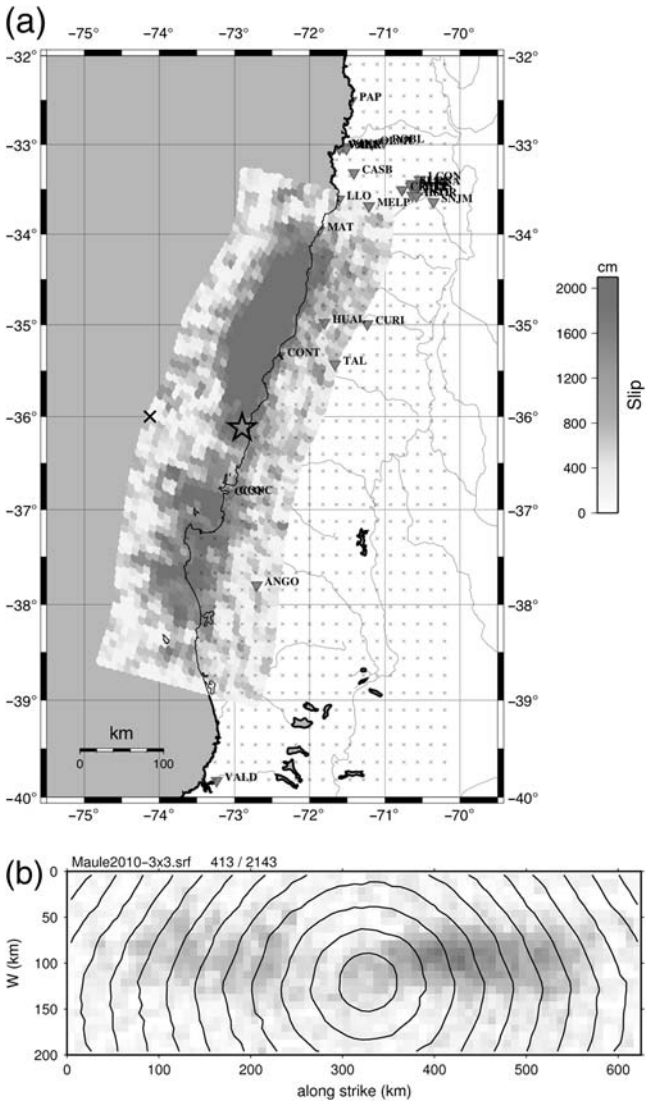

Figure 3. (a) Rupture model of the 2010 **M** 8.8 Maule, Chile, earthquake showing the slip distribution of Lorito *et al.* (2011), the locations of strong ground motion recording stations, and the grid of stations used for simulations. (b) Resampled rupture model used in the calculations. Slip values (in centimeters) indicated by gray shading. Contours of rupture initiation times across the fault plane are shown at 5 s intervals.

period-dependent amplification factors were used to scale the response spectra of the synthetic waveforms.

11 March 2011 **M** 9.0 Tohoku, Japan, Earthquake

Slip Model. Several rupture models have been proposed for this earthquake, estimated using strong-motion data (Kurahashi and Irikura, 2013), tsunami data (Fujii *et al.*, 2011; Hayashi *et al.*, 2011; Satake *et al.*, 2013), geodetic data (Yue and Lay, 2011), and combinations of all the previous types of rupture models (Koketsu *et al.*, 2011; Yokota *et al.*, 2011; Yoshida *et al.*, 2011). In this article, we chose to use the rupture model of Kurahashi and Irikura (2013) (Fig. 4a) that contains five strong-motion generating areas (SMGAs) with different sizes superimposed upon the larger rupture area of the earthquake. The characteristics as well as the locations of each SMGA are listed in Table 3. The total rupture dimensions of the earthquake were ~480-km-long along strike and 150-km-wide down-dip, significantly smaller than previous **M** ~ 9 megathrust earthquakes, which resulted in a high stress drop of 4.8 MPa (Koketsu *et al.*, 2011). Figure 4b shows the final rupture model used for broadband simulations. The original rupture model from Kurahashi and Irikura (2013) was modified to account for rupture times using the dependency of rupture velocity on slip.

Strong-Motion Records. The Tohoku earthquake produced an extensive number (~2000) of high-quality strong-motion recordings from a very dense network of accelerometers (K-Net, KiK-net). To validate the results of our simulation technique, we obtained the strong ground motion recordings from 44 stations, for which locations are shown in Figure 4a. The stations selected for the comparison were all fore-arc stations to avoid complex attenuation phenomena (Skarlatoudis and Papazachos, 2012; Stewart *et al.*, 2013) and were

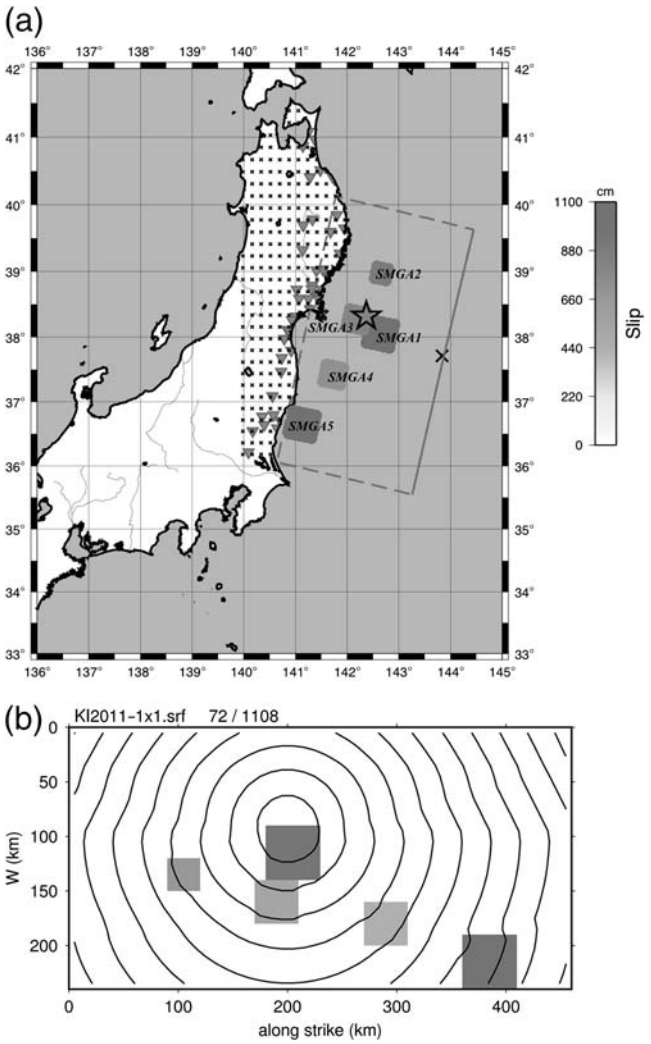

Figure 4. (a) Rupture model of the 2011 **M** 9.0 Tohoku, Japan, earthquake, showing the slip distribution of Kurahashi and Irikura (2013), the locations of strong ground motion recording stations, and the grid of stations used for simulations. (b) Resampled rupture model used in the calculations. Slip values (in centimeters) indicated by gray shading. Contours of rupture initiation times across the fault plane are shown at 5 s intervals.

part of the dataset that was used in deriving the Kurahashi and Irikura (2013) rupture model.

Crustal Structure Model. The crustal structure model that we used is based on the 3D velocity model for Japan derived by Koketsu *et al.* (2008). The 1D models for various sites were extracted from the 3D model, and the final model listed in Table 4 is an average of all these models. This model has a median V_{S30} of 309 m/s, and consequently all comparisons between the recordings and the synthetic waveforms are presented for sites with this V_{S30}. At the time that we were performing the study for the Tohoku event the amplification factors proposed by Boore *et al.* (2013) became available. We decided to use them instead of the NEHRP factors used in the studies of Arequipa and Maule events to scale the response spectra from recordings to the median V_{S30}.

Table 2
Crustal Structure Model for Chile

Thickness (km)	V_P (m/s)	V_S (m/s)	Density (kg/m^3)	Q_P*	Q_S*
0.2	2600	1500	2.00	40	20
6.7	5300	3030	2.10	200	100
4.6	6000	3370	2.50	500	200
18.1	6500	3650	2.78	500	200
15.8	7300	4100	3.18	1600	500

Modified from Ocola *et al.* (1995).
*Q is the anelastic attenuation factor for P and S waves (Q_P and Q_S), respectively.

Table 3
Source Parameters of Strong-Motion Generating Areas (SMGAs)

	Length (km)	Width (km)	M_0 (N·m)	Stress Drop (MPa)	Delay time from Origin Time (s)
SMGA 1	62.40	41.60	2.31×10^{21}	41.3	15.64
SMGA 2	41.60	41.60	7.05×10^{20}	23.6	66.42
SMGA 3	93.60	52.00	4.34×10^{21}	29.5	68.41
SMGA 4	38.50	38.50	3.83×10^{20}	16.4	109.71
SMGA 5	33.60	33.60	3.99×10^{20}	26.0	118.17

Source: Kurahashi and Irikura (2013).

Table 4
Crustal Structure Model for Japan

Thickness (km)	V_P (m/s)	V_S (m/s)	Density (kg/m^3)	Q_P	Q_S
0.002	1700	450	2.00	45.0	22.5
0.004	1800	650	2.10	65.0	32.5
0.006	1800	850	2.10	85.0	42.5
0.008	1900	950	2.10	95.0	47.5
0.01	2000	1150	2.20	115.0	57.5
0.07	2400	1200	2.20	120.0	60.0
0.10	2600	1300	2.40	130.0	65.0
0.16	3000	1400	2.45	140.0	70.0
0.10	3600	2000	2.55	200.0	100.0
0.44	4200	2400	2.60	240.0	120.0
5.90	5500	3200	2.65	320.0	160.0
10.20	6100	3400	2.75	340.0	170.0
14.63	6500	3800	3.00	380.0	190.0
16.00	7800	4500	3.30	450.0	225.0

Modified by Koketsu *et al.* (2008).

Goodness-of-Fit Comparisons

The comparisons between the recordings and the simulations at all stations for all three earthquakes studied are quantified using the response spectral goodness of fit (GOF). The residual between the observed and simulated spectral acceleration at a period T_i for the jth station is given by

$$r_j(T_i) = \ln\left[\frac{O_j(T_i)}{S_j(T_i)}\right], \quad (4)$$

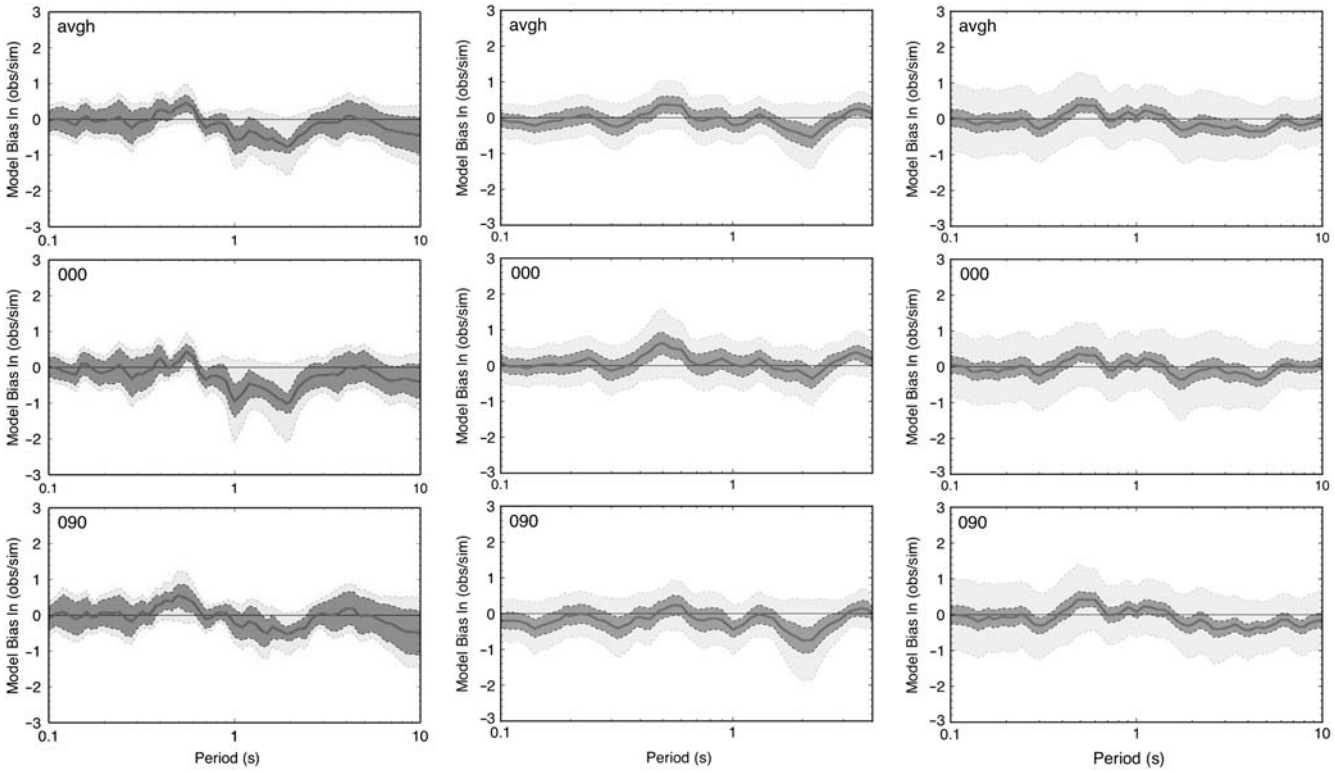

Figure 5. Goodness of fit (GOF) of recorded and simulated response spectra for the 0.1–10 s period range for the (left) 2001 Arequipa, (middle) 2010 Maule, and (right) 2011 Tohoku earthquakes. The top panels show the GOF for the average horizontal component, the middle panels show the GOF for the north–south component, and the bottom panels show the GOF for the east–west component of ground motion. The solid line shows the bias, the light gray zone shows the standard deviation, and the dark gray zone shows the 90% confidence interval of the mean.

in which $O_j\ (T_i)$ and $S_j\ (T_i)$ are the observed and simulated values for a given component, respectively. The model bias is then given by

$$B(T_i) = \frac{1}{N}\sum_{j=1,N} r_j(T_i), \tag{5}$$

and the standard error is given by

$$\sigma(T_i) = \left\{\frac{1}{N}\sum_{j=1,N}[r_j(T_i) - B(T_i)]^2\right\}^{1/2}, \tag{6}$$

following the notation of Graves and Pitarka (2010).

In Figure 5, the GOF plots for the (left) Arequipa 2001, (middle) Maule 2008, and (right) Tohoku 2011 earthquakes are presented. The top panels correspond to the GOF for the average horizontal component of ground motion, whereas the middle and bottom panels correspond to the north–south and east–west components, respectively. The solid line shows the bias, the light gray zone shows the bias $\pm$ 1 standard deviation, and the dark gray zone shows the 90% confidence interval of the mean.

These comparisons show little systematic bias in the prediction of the ground motions, although there is some underprediction at a period of 0.5 s for all three simulations. Simulations for Maule and Tohoku perform relatively better than the Arequipa ones at periods around 1 s, in which the simulations tend to overpredict. The standard deviation of the prediction (shown by the gray shading) is about a factor of 1.5 (0.4 natural log units).

Comparisons with Ground-Motion Prediction Models

The ground-motion estimates obtained for each earthquake were compared with two ground-motion prediction equations (GMPEs) for subduction earthquakes, the Zhao *et al.* (2006, hereafter referred to as Zhao06) and the Abrahamson *et al.* (2015, hereafter referred to as AGA12). The AGA12 model was derived from a worldwide set of strong-motion recordings of subduction earthquakes. The Zhao06 model was derived from strong-motion recordings from both crustal and subduction earthquakes in Japan. These comparisons are presented in two different ways; as response spectra amplitudes plotted against distance for a set of spectral periods and against spectral period for a set of distance bins.

The average horizontal response spectra of the simulations of the 2001 Arequipa earthquake are compared with the ground-motion models in a suite of spectral periods and distance ranges for soft rock (B/C site condition) in Figures 6 and 7. For the B/C site condition, we use a V_{S30} of 760 m/s and for the Zhao06 model the site class terms for the soil category SC I (rock/stiff soil; $V_{S30} > 600$ m/s). The closest agreement is obtained for the Zhao06 model. For the 2008 Maule earthquake, the agreement between the simulations and both the Zhao06 and AGA12 ground-motion models

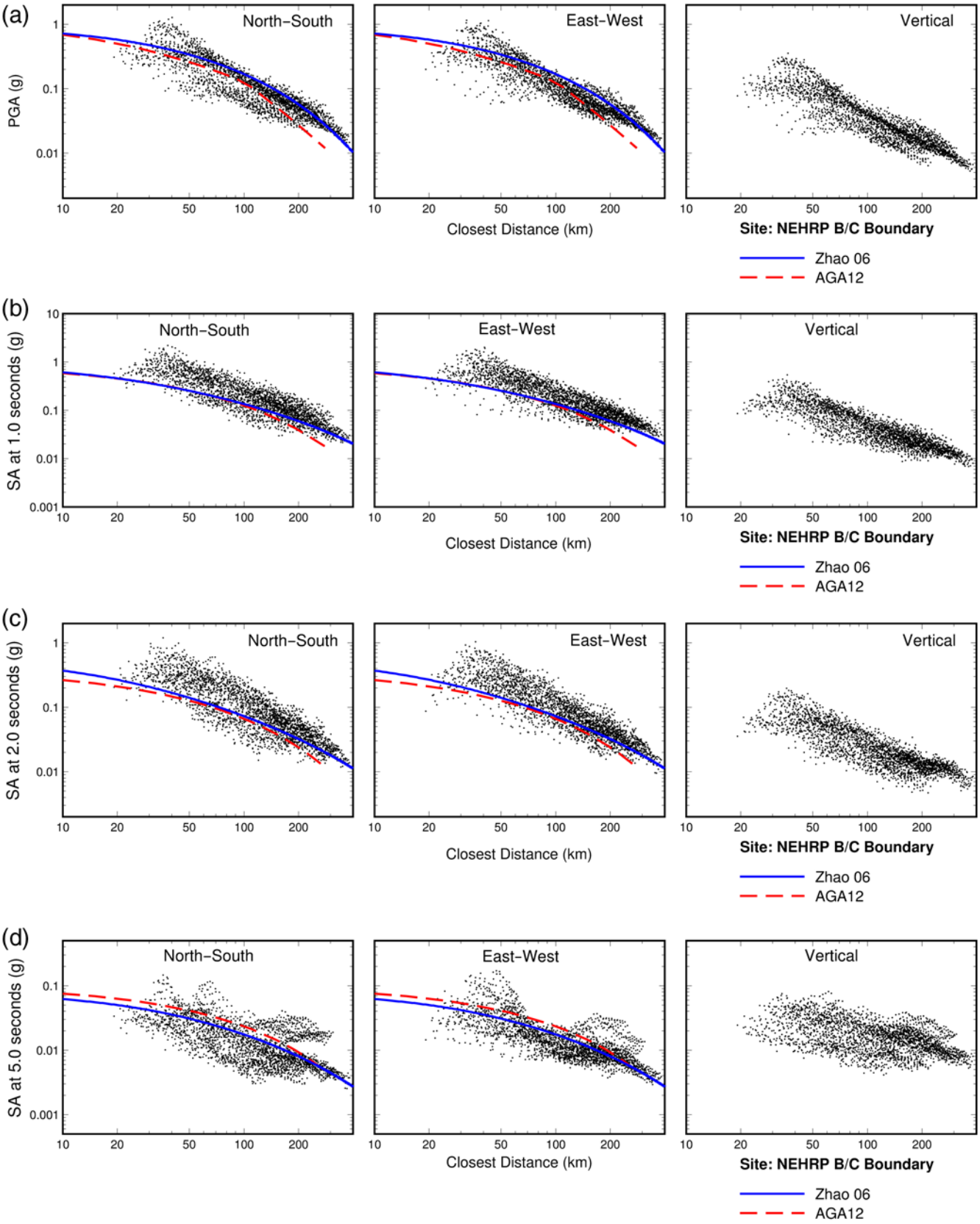

Figure 6. Comparison of simulated peak ground acceleration (PGA) and 1, 2, and 5 s spectral accelerations for the 2001 Arequipa, Peru, earthquake with Zhao *et al.* (2006, hereafter referred to as Zhao06; solid curve) and Abrahamson *et al.* (2012, hereafter referred to as AGA12; dashed curve) ground-motion models for soft-rock (National Earthquake Hazards Reduction Program [NEHRP] B/C boundary) site conditions. The color version of this figure is available only in the electronic edition.

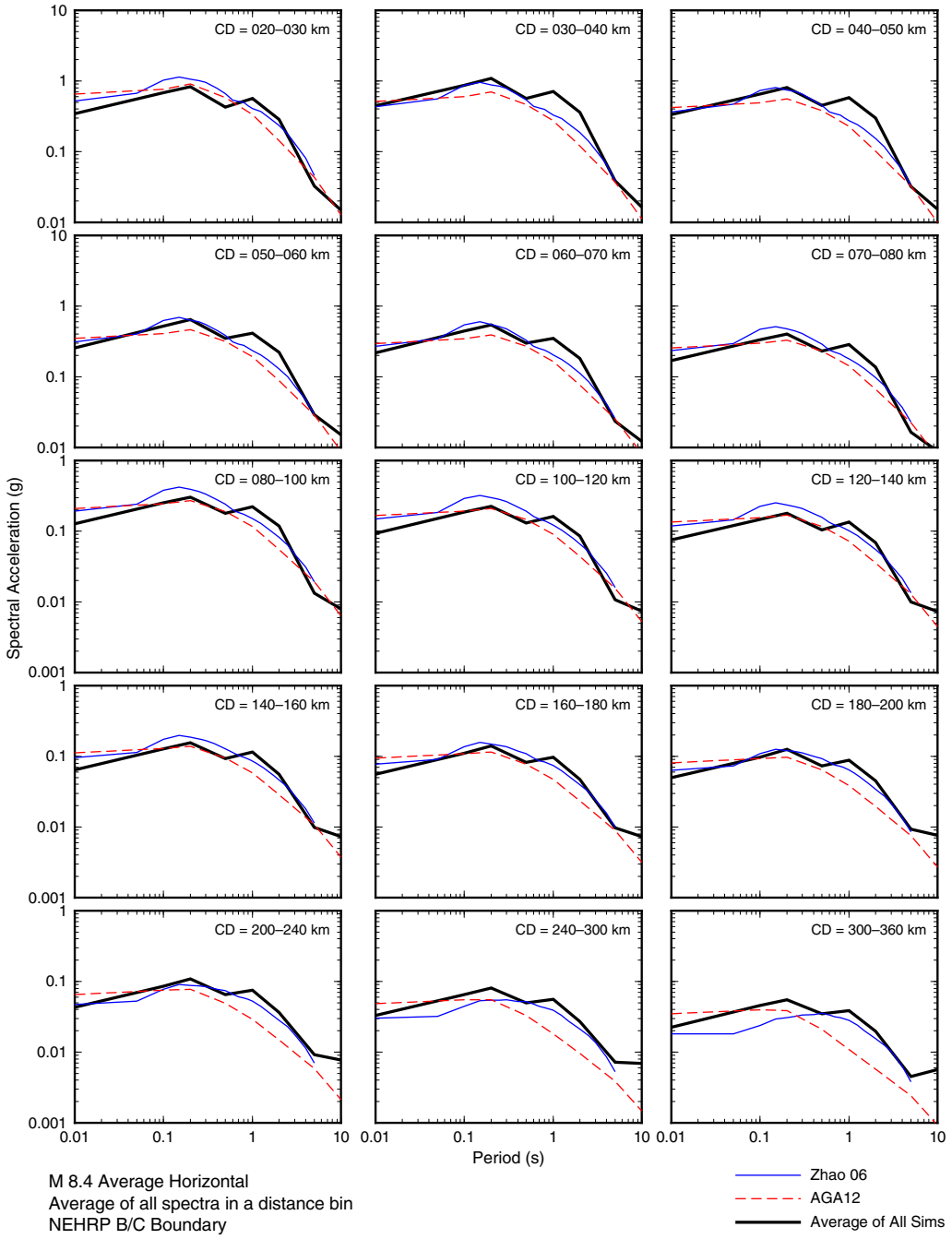

Figure 7. Comparison of average horizontal simulated response spectra for a suite of distance ranges for the 2001 Arequipa, Peru, earthquake for soft-rock (NEHRP B/C boundary) site conditions with two ground-motion models. The color version of this figure is available only in the electronic edition.

is quite close for peak acceleration. At 1 and 2 s, the simulations are in very good and fairly good agreement with the models, as shown in Figures 8 and 9. In Figure 10, a similar comparison for the 2011 Tohoku is shown. The agreement between the simulations and GMPEs is quite close for shorter periods. However, at a period of 2 s the simulations exhibit lower values and a steeper attenuation trend than those predicted by the empirical models for distances larger than 30 km. Looking at the spectral amplitude decay in Figure 11, the steeper attenuation of ground motions at longer periods is more prominent for distances between 40 and 80 km, but in general there is good agreement with the Zhao06 model. These differences may be attributable to the simple 1D Green's functions that were computed by our method, which might not be able to capture the full complexity of the source rupture and wave propagation, but the overall performance of the method and the unbiased results shown in the GOF plot of Figure 5 demonstrate our capability to simulate broadband ground motions from this event.

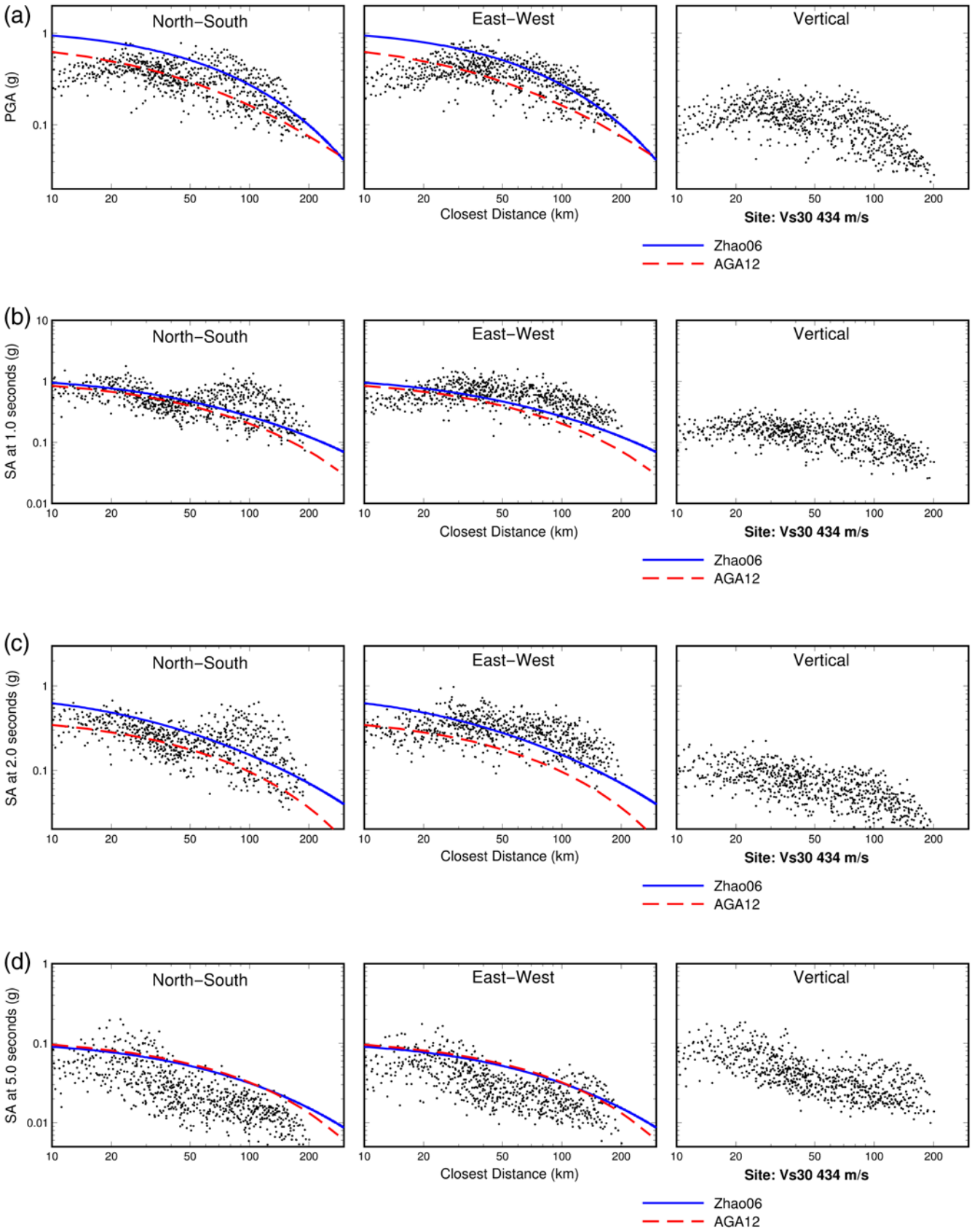

Figure 8. Comparison of simulated PGA and 1, 2, and 5 s spectral accelerations for the 2010 Maule, Chile, earthquake with Zhao06 (solid curve) and AGA12 (dashed curve) ground-motion models for sites with $V_{S30} = 434$ m/s. The color version of this figure is available only in the electronic edition.

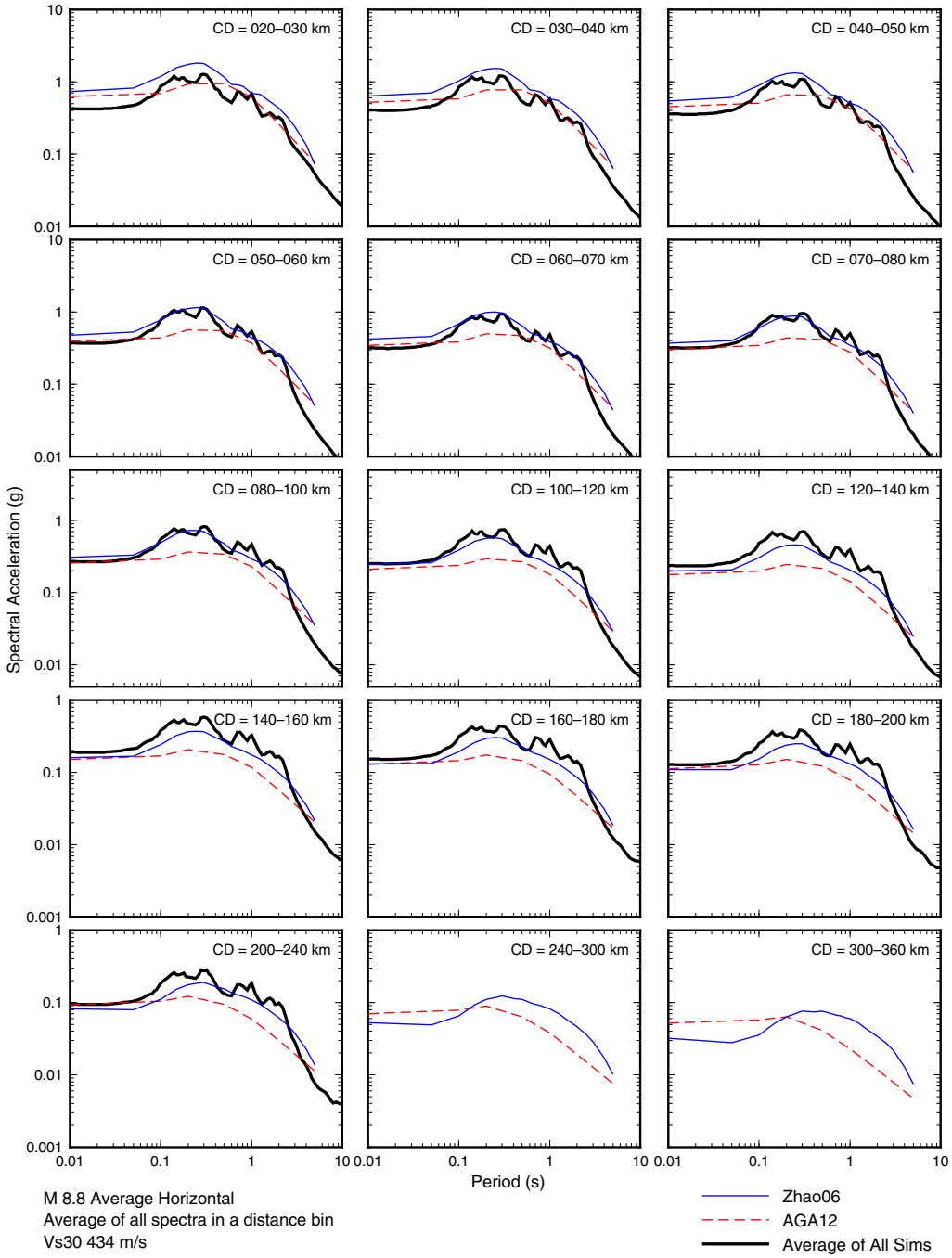

Figure 9. Comparison of average horizontal simulated response spectra for a suite of distance ranges for the 2010 Maule, Chile, earthquake for sites with $V_{S30} = 434$ m/s with two ground-motion models. The color version of this figure is available only in the electronic edition.

Earthquakes That Rupture the Entire Cascadia Subduction Zone

For these case studies, we validated the method against recorded ground motions and empirical prediction models. Because the method demonstrated a fairly good ability to reproduce the ground motions of these major subduction earthquakes, we applied the method to generate ground motions for the Cascadia subduction zone.

Earthquake Source Characterization

The geometry of the Cascadia earthquake source models used in this study was based on the source characterization of Petersen *et al.* (2008). In particular, we used their "base" model of the bottom of the seismogenic plate interface (shown in Fig. 12a), to which they gave a weight of 0.5. This model is based on the global observation that rupture usually extends down to depths of ~30 km. Petersen *et al.* (2008)

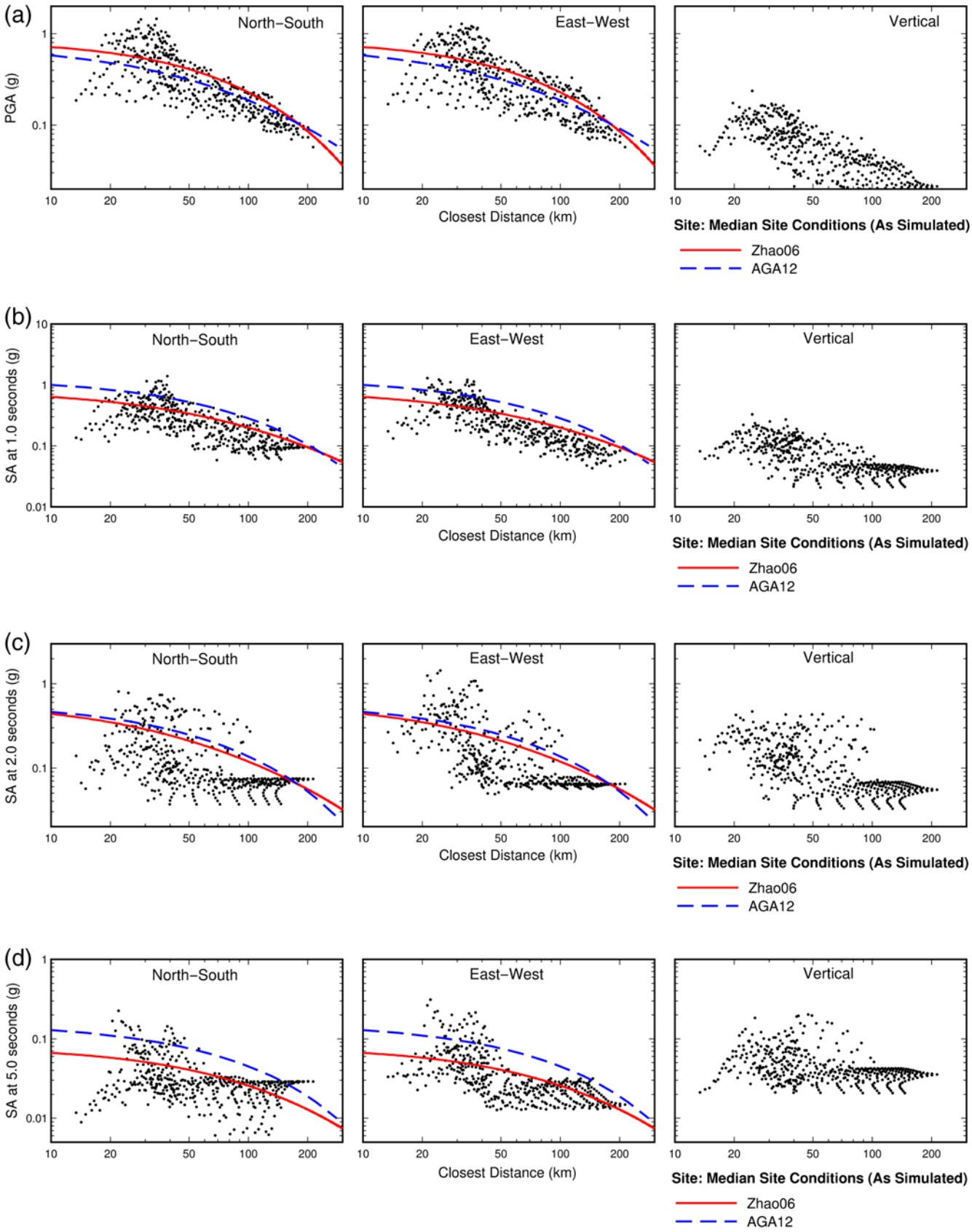

Figure 10. Comparison of simulated PGA and 1, 2, and 5 s spectral accelerations for the 2011 Tohoku, Japan, earthquake with Zhao06 (solid curve) and AGA12 (dashed curve) ground-motion models for sites with $V_{S30} = 309$ m/s. The color version of this figure is available only in the electronic edition.

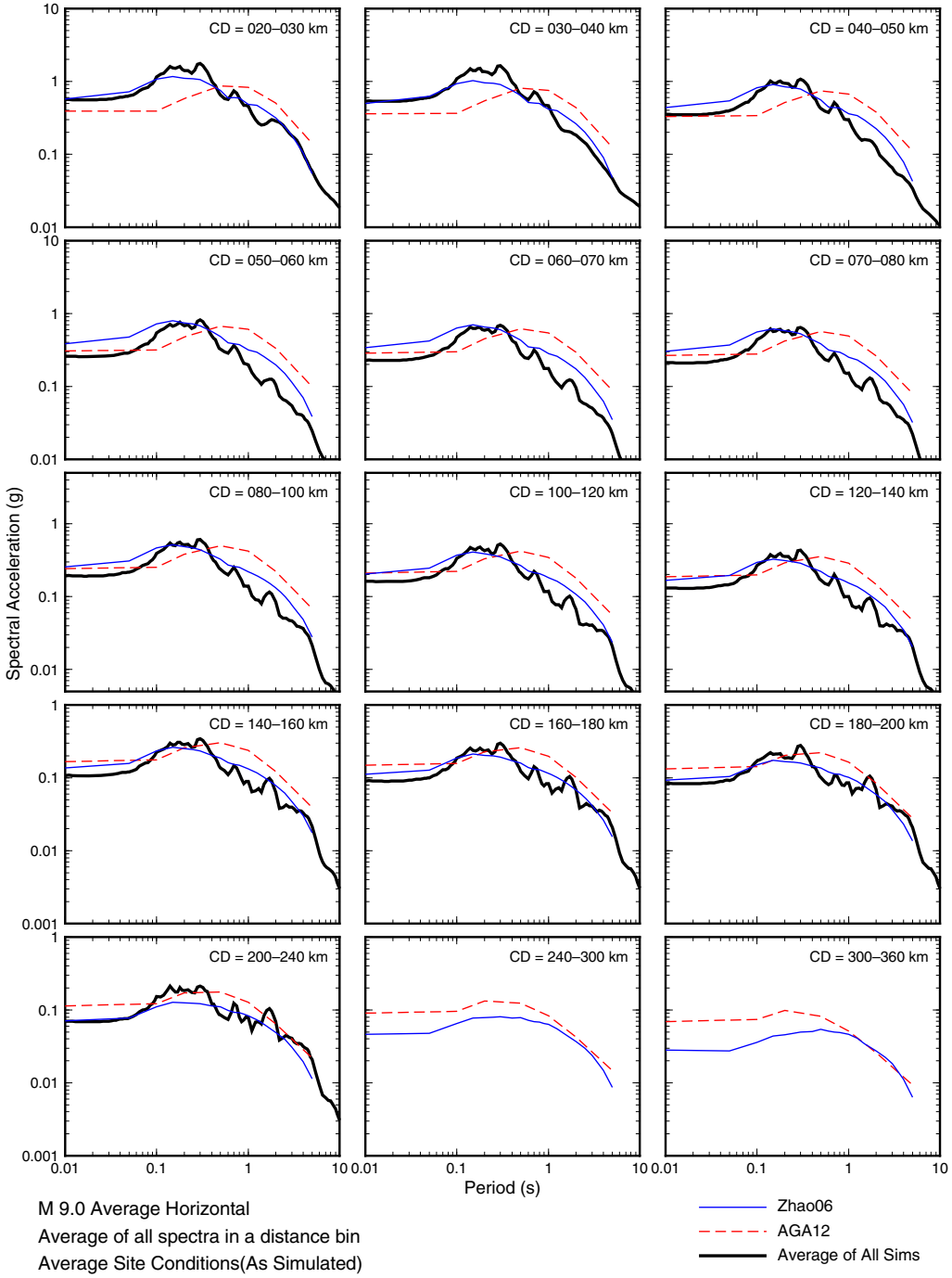

Figure 11. Comparison of average horizontal simulated response spectra for a suite of distance ranges for the 2011 Tohoku, Japan, earthquake for sites with $V_{S30} = 309$ m/s with two ground-motion models. The color version of this figure is available only in the electronic edition.

used alternative models to describe the surficial expression of the trench: top, base of the elastic zone; mid, midpoint of the transition zone; bottom, base of the transition zones, which are also shown in Figure 12. The sensitivity of the calculated seismic hazard to uncertainty in the model for the bottom of the seismogenic zone was analyzed by Petersen *et al.* (2002). This depth controls the eastern extent of the subduction source and thus has a strong influence on ground-motion levels in the urban regions of Washington and Oregon, which mainly lie to the east of the source.

The fault geometry used to represent the base model is shown in Figure 12b. The subduction interface was divided into three segments to accommodate the shallower dip at the bend in the subduction zone near the Olympic Peninsula. The shallower segment has a down-dip width of 160 km, whereas the other segments have down-dip widths of 120 km. The

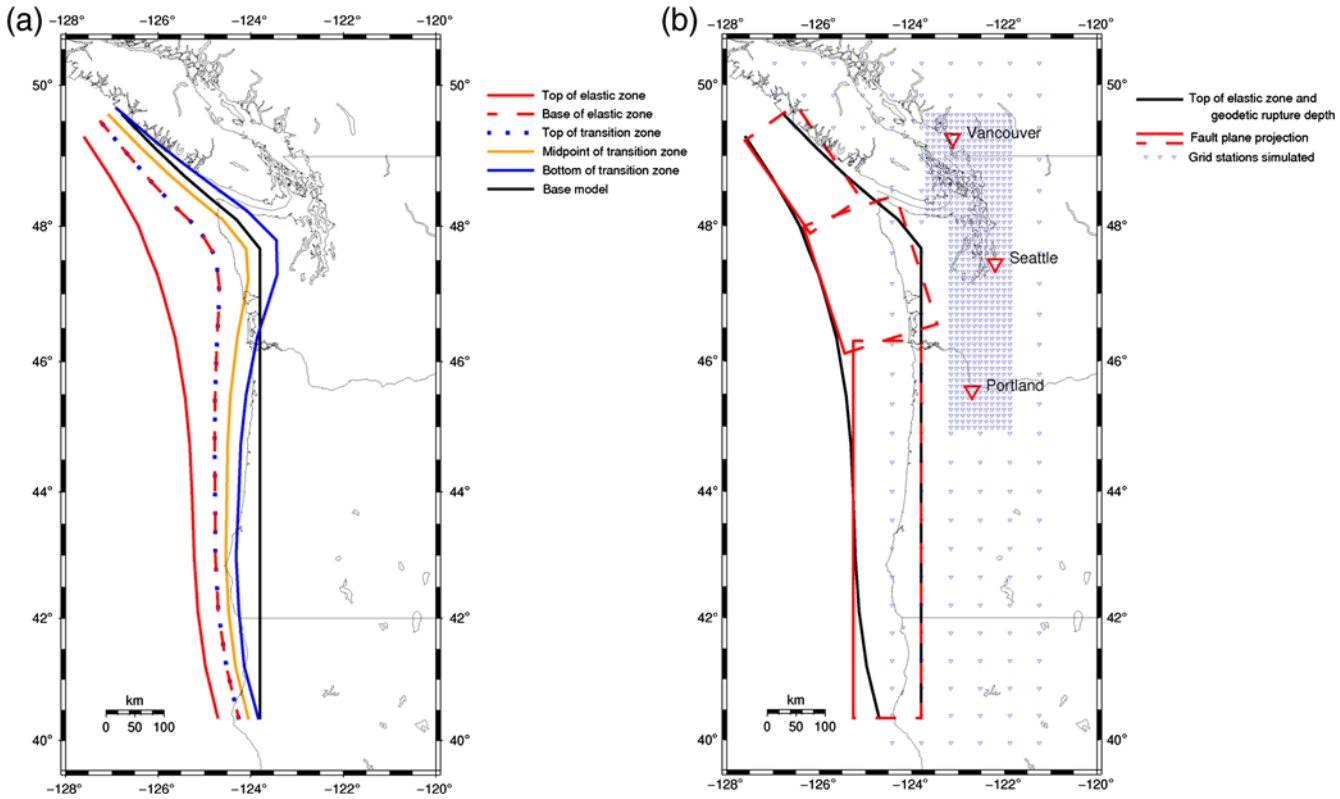

Figure 12. (a) Alternative models of the down-dip extent of the Cascadia subduction zone (from Petersen *et al.*, 2008). This study used the base model based on global data, shown by the thick black line. (b) Modeled rupture geometry of the Cascadia subduction zone and the grid of stations used for strong-motion simulation (small triangles). The locations of the cities (large triangles) are also part of the denser grid of stations. The color version of this figure is available only in the electronic edition.

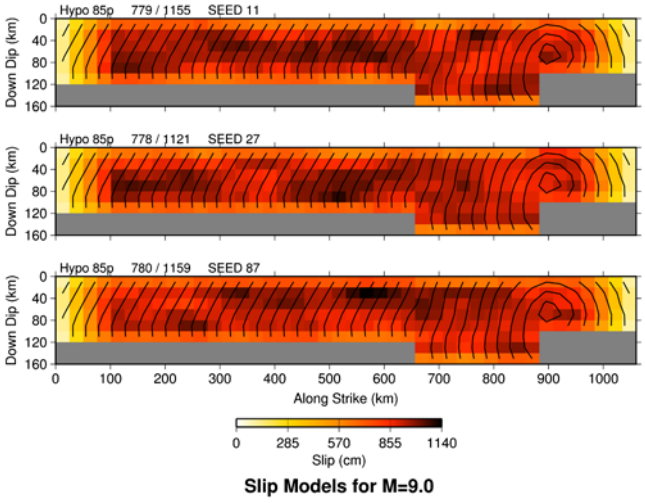

Figure 13. Rupture models of **M** 9.0 scenario earthquakes on the Cascadia subduction zone having northern hypocenters. The slip values of all models are the same for the different hypocenters (southern, central, and northern). The color version of this figure is available only in the electronic edition.

rupture area of the combined fault segments is 131,500 km^2. Petersen *et al.* (2008) assume that such earthquakes have magnitudes in the 8.8–9.2 range, with a weight of 0.6 given to magnitude 9.0 and weights of 0.2 given to magnitudes of 8.8 and 9.2. A rupture area of 131,500 km^2 corresponds to **M** 8.96 in the Murotani *et al.* (2013) relations. Based on this and the recent megathrust earthquakes that occurred worldwide, we used **M** 9.0 to represent the magnitude of a subduction earthquake that ruptures the entire 131,500 km^2 of the Cascadia subduction interface.

Table 5
Crustal Structure Model for Cascadia

V_P (km/s)	Q_P	V_S (km/s)	Q_S	Density (kg/m^3)	Thickness (km)
2.600	2000	1.500	900.0	2.000	0.20
5.300	2000	3.030	900.0	2.100	6.70
6.000	2000	3.370	900.0	2.500	4.60
6.500	2000	3.650	900.0	2.780	18.10
7.300	2000	4.100	900.0	3.180	15.80
8.100	2000	4.500	900.0	3.400	16.00
8.101	2000	4.501	900.0	3.401	100.00

For the scenario event with magnitude **M** 9.0 (rupture area, 131,500 km^2; average slip, 831 cm; rise time, 12.7 s; and slip velocity, 66 cm/s), we generated more than 100 different earthquake rupture models, for three different hypocentral locations (i.e. south, central, and north), to study the variability and the sensitivity of the derived ground motions to the individual characteristics of each slip model used. We selected three slip models (11, 27, and 87) for producing ground-motion simulations.

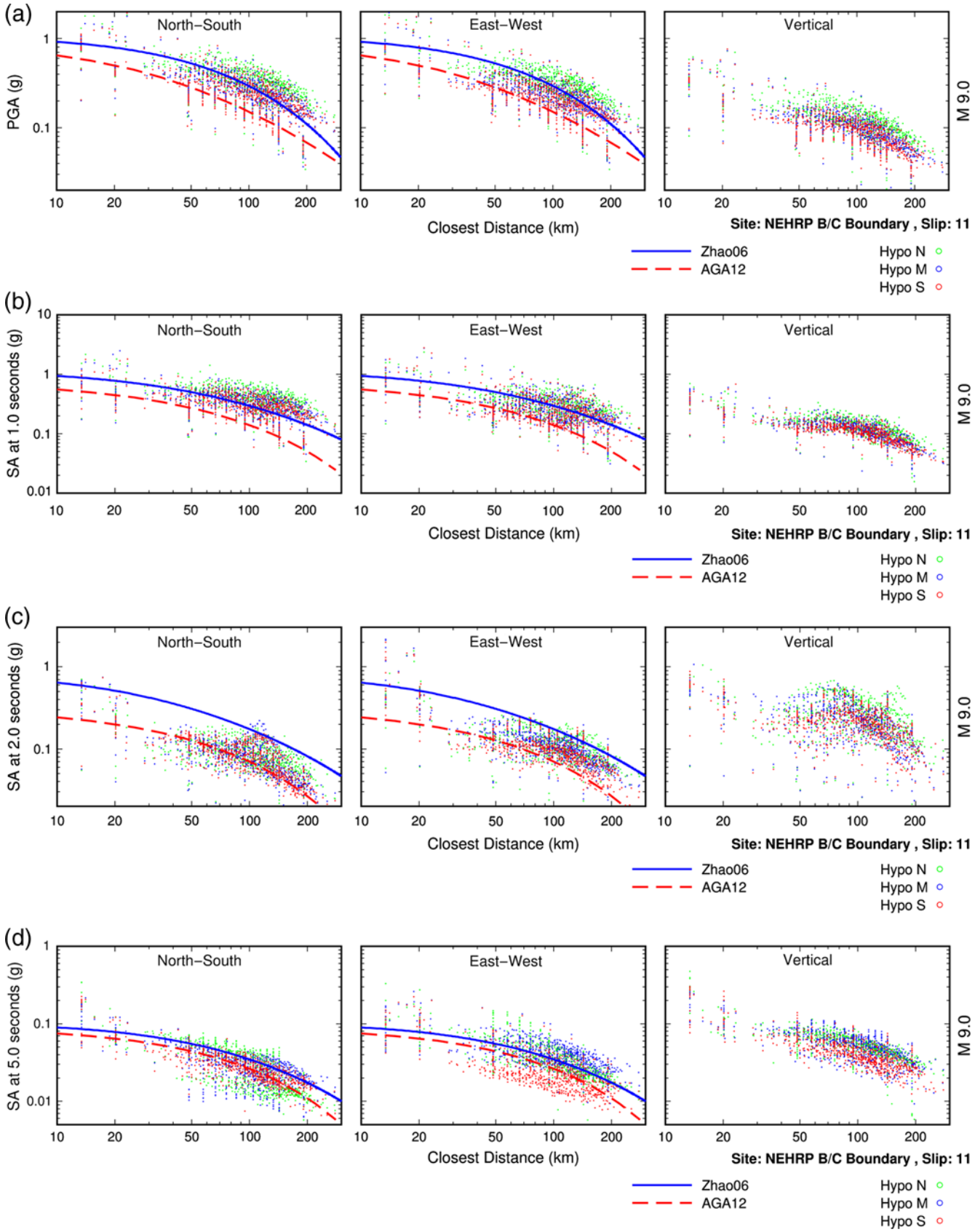

Figure 14. Comparison of simulated PGA and 1, 2, and 5 s spectral accelerations for **M** 9.0 Cascadia earthquake with Zhao06 (solid curve) and AGA12 (dashed curve) ground-motion models for soft-rock (NEHRP B/C boundary) site conditions. The color version of this figure is available only in the electronic edition.

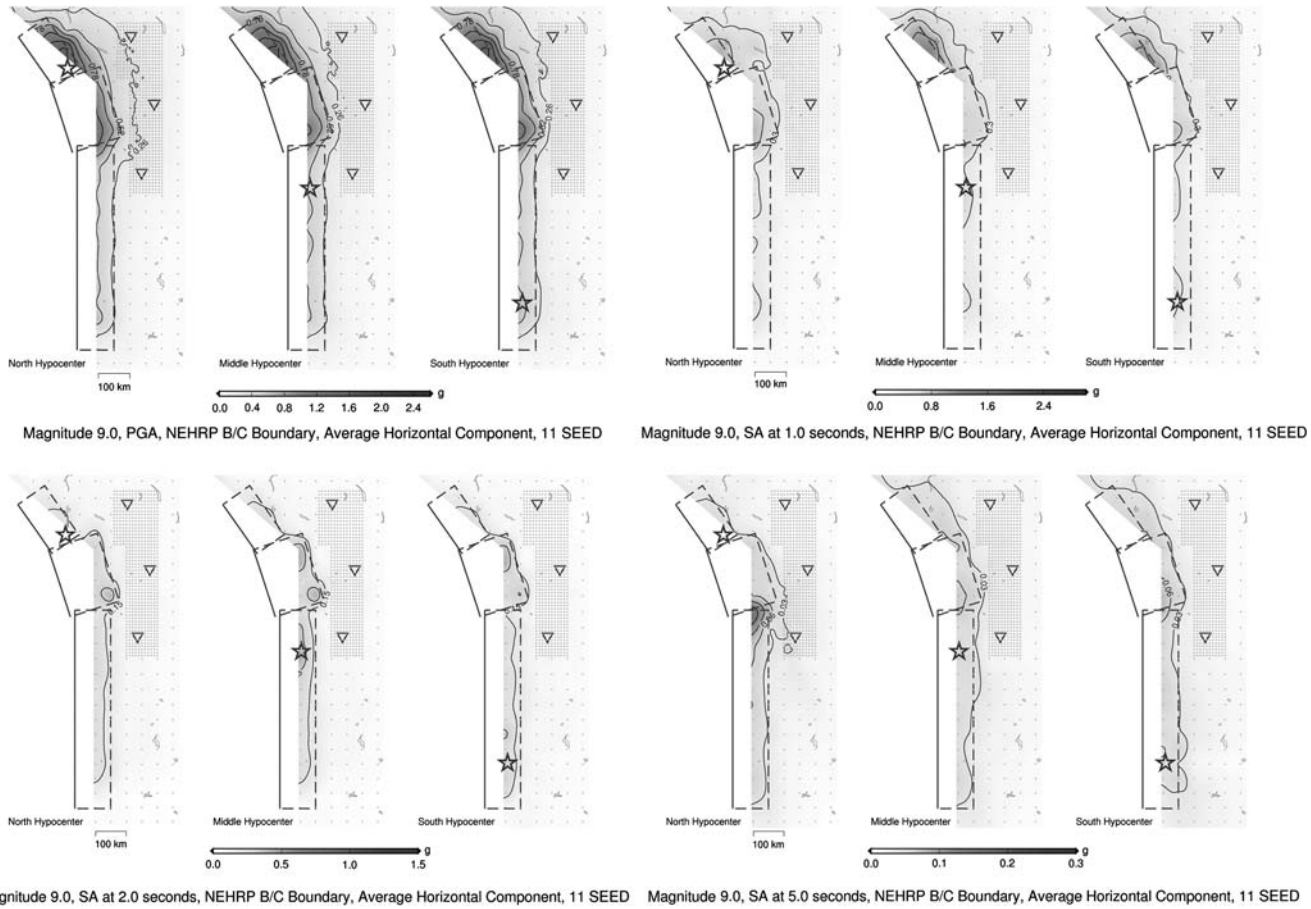

Figure 15. Ground-motion maps for PGA and 1, 2, and 5 s spectral acceleration, for an **M** 9.0 Cascadia earthquake for three hypocenter locations and for NEHRP B/C boundary site conditions.

All three models have very similar average slip values, although there are differences in the spatial distribution of slip, mostly down-dip of the fault. For model 11, the slip is uniformly distributed along the fault; whereas for 27 and 87, the highest slip values are concentrated in the lower and upper parts of the fault, respectively. The rupture models of the **M** 9.0 event for the north hypocenter are shown in Figure 13.

Crustal Structure

To represent the crustal structure of the study area, we used the velocity model shown in Table 5, which we found broadly compatible with the velocity model for Cascadia described by McNeill *et al.* (2004). Based on several earlier studies that demonstrated the adequacy of Green's functions computed using a series of 1D approximations to 2D (e.g., Cohee *et al.*, 1991; Somerville *et al.*, 2003, 2013a,b) or 3D ones (e.g., McNeill *et al.*, 2004), we decided to use Green's functions computed using a 1D approximation to the velocity model of the Cascadia subduction zone.

Another important influence on the amplitude and durations on strong ground motions is the effect of sedimentary basins, such as the Puget trough and the Portland and Tualatin basins. We recognize that this is an important issue to be addressed in future studies, but it lies beyond the scope of this article.

Ground-Motion Maps

We performed ground-motion simulations at the stations shown by the grid in Figure 12 following the same procedure as for the three case studies. The three rupture scenarios we selected produced very similar ground motions; and, therefore, we present results just for slip model 11. An example of the computed ground motions is shown in Figure 14, which compares forward simulations for an **M** 9.0 Cascadia earthquake with current GMPE models (Zhao06 and AGA12) for different spectral periods (peak ground acceleration [PGA], 1, 2, and 5 s). Larger variability is observed for higher frequencies (PGA), which gradually diminishes at longer periods.

The maps, shown in Figures 15, are for peak acceleration and response spectral acceleration at 1.0, 2.0, and 5.0 s for the same slip model and for NEHRP B/C boundary site conditions. The highest values for PGA cover a broad area of the Olympic Peninsula, independent of the hypocentral location of the scenario earthquake. However, for the longer periods of ground motion ($T > 1$ s), the maximum values

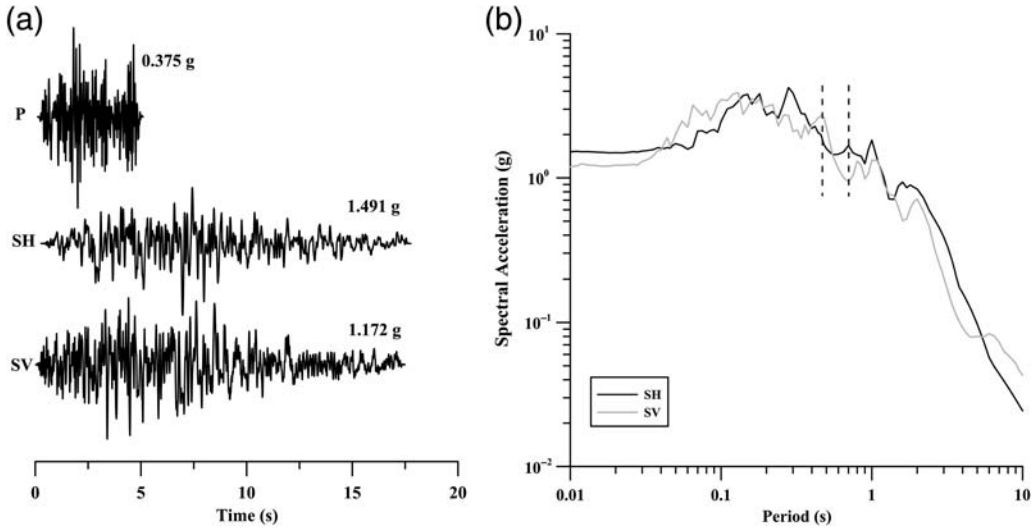

Figure 16. (a) Empirical source function time histories derived from the Caleta de Campos recording of the 30 April 1986 Michoacan aftershock. (b) Response spectra of the *SH* and *SV* components of ground motion. The vertical dashed lines depict the 0.4–0.7 s period range.

of ground motion can be identified in a well-defined coastal zone that extends from Washington to the northern parts of California.

Discussion and Conclusions

Figure 5 shows the spectral acceleration modeling bias for the three earthquakes we have examined. For all events, the simulations have a model bias generally less than a factor of 1.2 across the full bandwidth. A systematic underprediction can be observed around the period of 0.5 s in all three bias plots. This underprediction could be caused by the characteristics of the emprical source function used in the high-frequency part of the simulations. Figure 16 shows the response spectra of the vertical and radial components from the Caleta de Campos recording of the 1986 Michoacan, Mexico, earthquake. It can be seen that for the radial components there is a small trough in the 0.4–0.7 s period range (depicted with the vertical dashed lines in Fig. 16b) which could explain the underprediction in our simulations in that period range.

The modeling errors, represented by the standard deviation for spectral acceleration (from equation 6) for the three earthquakes we have examined and the corresponding measures computed from the two GMPE models used in the individual earthquake simulation evaluations, are shown in Figure 17. For the Arequipa earthquake, the simulations have standard deviation of around 0.5 (natural log units) showing a trend to higher values for periods longer than 3 s. Similar results are shown for the Maule earthquake, although the comparisons are limited to periods up to 4 s due to data limitations. The standard deviation for the Tohoku earthquake exhibits somewhat higher values than the other two earthquakes, although it is fairly constant across the examined period range and comparable with the standard deviations of the most recent GMPE models (Zhao06 and AGA12). The Zhao06 model has very comparable values for almost the whole period range examined.

Because our simulation methodology produces broadband time series, the resulting ground motions can be used in many different ways. Despite the various uncertainties in the comparisons shown in Figures 14 and 15, broadband simulations can be useful in assessing certain characteristcs of ground motions from megathrust earthquakes in subduction zones like Cascadia that lack observations.

The validation results presented here demonstrate the ability of the hybrid simulation methodology to reproduce the main characteristics of the observed ground motions for megathrust earthquakes over a broad frequency range.

Data and Resources

All the information regarding the K-Net and KiK-net recording stations is available from the National Research Institute for Earth Science and Disaster Prevention of Japan (NIED; http://www.kyoshin.bosai.go.jp, last accessed May 2015). Some plots were created using the Generic Mapping Tools v.4.2.1 (www.soest.hawaii.edu/gmt, last accessed November 2013; Wessel and Smith, 1998).

Acknowledgments

We would like to thank Kojiro Irikura and the anonymous reviewer for their thorough reviews and important comments, which significantly improved the manuscript. Research on the Arequipa, Maule, and Tohoku earthquakes was supported by the U.S. Geological Survey (USGS), Department of the Interior, under USGS Award Numbers (06HQGR0160, G11AP20041, and G12AP20081 to P. Somerville). The views and conclusions contained in this document are those of the authors and should not be interpreted as necessarily representing the official policies, either expressed or implied, of the U.S. Government.

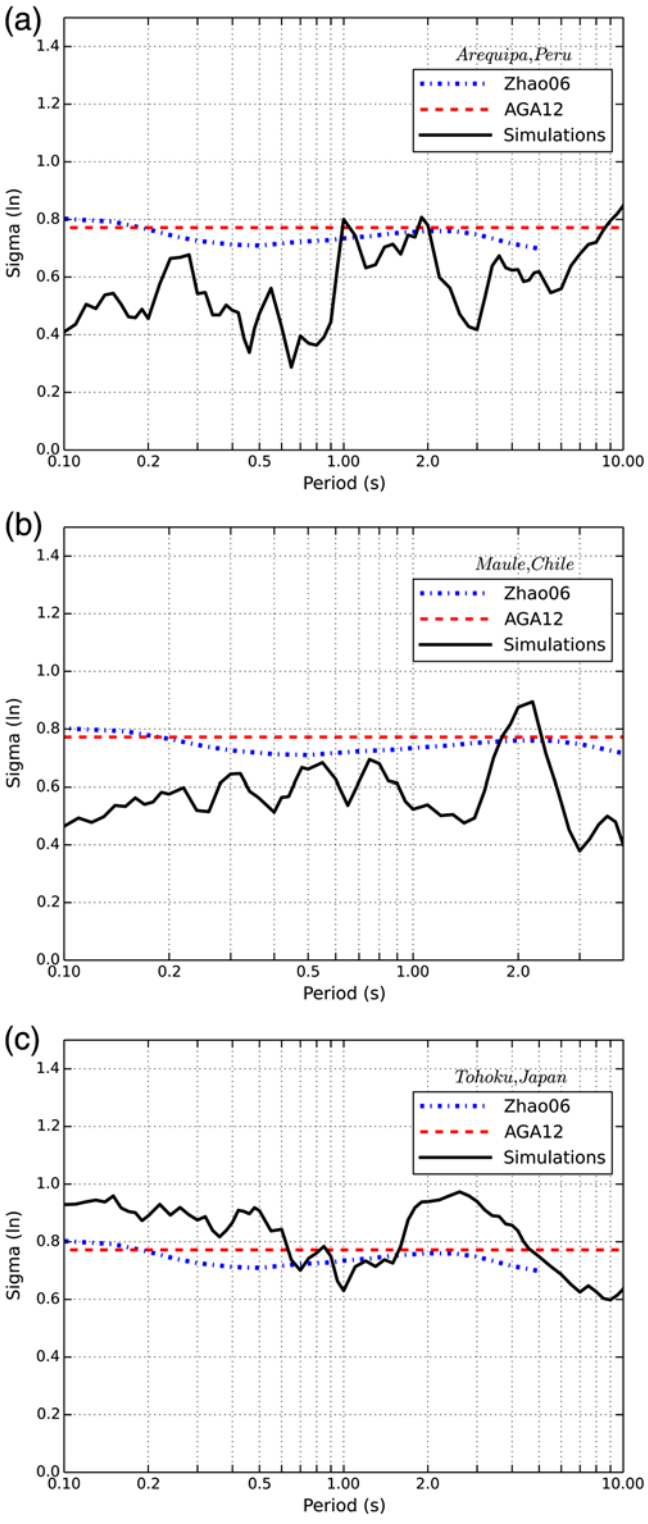

Figure 17. Comparison of spectral acceleration standard error for our simulations for (a) Arequipa, Peru; (b) Maule, Chile; and (c) Tohoku, Japan, earthquakes with that obtained from empirical ground-motion prediction equations (GMPEs) for subduction areas. The Zhao06 and AGA12 GMPEs are used in the comparisons. The color version of this figure is available only in the electronic edition.

References

Abrahamson, N., N. Gregor, and K. Addo (2015). BC Hydro ground motion prediction equations for subduction earthquakes, *Earthq. Spectra* doi: 10.1193/051712EQS188MR (in press).

Atkinson, G. M., and D. M. Boore (2003). Empirical ground motion relations for subduction zone earthquakes and their application to Cascadia and other regions, *Bull. Seismol. Soc. Am.* **93,** 1703–1729.

Boore, D. M., J. P. Stewart, E. Seyhan, and G. M. Atkinson (2013). NGA-West2 equations for predicting response spectral accelerations for shallow crustal earthquakes, *PEER Report*, May 2013, 135 pp.

Boroschek, R., and D. Comte (2004). Time–frequency characteristics of the 2001 southern Peru, M_w 8.4 earthquake, *13th World Conference on Earthquake Engineering*, Vancouver, British Columbia, 1–6 August 2004, Paper Number 287.

Boroschek, R., and V. Contreras (2012). Strong ground motion from the 2010 M_w 8.8 Maule Chile earthquake and attenuation relations for Chilean subduction zone interface earthquakes, *International Symposium on Engineering Lessons Learned from the 2011 Great East Japan Earthquake*, Tokyo, Japan, 1–4 March 2012.

Building Seismic Safety Council (BSSC) (2003). *National Earthquake Hazards Reduction Program Recommended Provisions and Commentary for Seismic Regulations for New Buildings and Other Structures (FEMA 450)*, Part 1, Federal Emergency Management Agency (FEMA), Washington, D.C., 2013 Edition.

Cohee, B. P., P. G. Somerville, and N. A. Abrahamson (1991). Ground motions from hypothesized $M_w = 8$ subduction earthquakes in the Pacific Northwest, *Bull. Seismol. Soc. Am.* **81,** 28–56.

Fujii, Y., K. Satake, S. Sakai, M. Shinohara, and T. Kanazawa (2011). Tsunami source of the 2011 off the Pacific coast of Tohoku earthquake, *Earth Planets Space* **63,** 815–820.

Graves, R. W., and A. Pitarka (2004). Broadband time history simulation using a hybrid approach, *Proceedings of the 13th World Conference on Earthquake Engineering*, Vancouver, Canada, 1–6 August 2004, Paper Number 1098.

Graves, R. W., and A. Pitarka (2010). Broadband ground-motion simulation using a hybrid approach, *Bull. Seismol. Soc. Am.* **100,** 2095–2123.

Guatteri, M., P. M. Mai, G. Beroza, and J. Boatwright (2003). Strong ground motion prediction from stochastic-dynamic source models, *Bull. Seismol. Soc. Am.* **93,** 301–313.

Hartzell, S. (1978). Earthquake aftershocks as Green's functions, *Geophys. Res. Lett.* **5,** 1–4.

Hartzell, S., and T. Heaton (1983). Inversion of strong ground motion and teleseismic waveform data for the fault rupture history of the 1979 Imperial Valley, California earthquake, *Bull. Seismol. Soc. Am.* **73,** 1553–1583.

Hayashi, Y., H. Tsushima, K. Hirata, K. Kimura, and K. Maeda (2011). Tsunami source area of the 2011 Off the Pacific Coast of Tohoku earthquake determined from tsunami arrival times at offshore observation stations, *Earth Planets Space* **63,** 809–813.

Hisada, Y. (2001). A theoretical omega-squared model considering spatial variation in slip and rupture velocity. Part 2. Case for a two-dimensional source model, *Bull. Seismol. Soc. Am.* **91,** 651–666.

Ichinose, G. A., H. K. Thio, P. G. Somerville, T. Sato, and T. Ishii (2003). Rupture model for the 1944 Tonankai earthquake from the inversion of teleseismic and regional seismograms, *J. Geophys. Res.* **108,** no. 10, 2497.

Irikura, K. (1978). Semi-empirical estimation of strong ground motions during large earthquakes, *Bull. Disast. Prev. Res. Inst. Kyoto Univ.* **63,** 104.

Ishii, T., T. Sato, and P. G. Somerville (2000). Identification of main rupture areas of heterogeneous fault models for strong motion estimates, *J. Struct. Constr. Eng.* **527,** 61–70.

Koketsu, K., H. Miyake, H. Fujiwara, and T. Hashimoto (2008). Progress towards a Japan integrated velocity structure model and long-period ground motion hazard map, presented at *14th World Conference on Earthquake Engineering*, Beijing, China, Paper Number S10-038.

Koketsu, K., Y. Yokota, N. Nishimura, Y. Yagi, S. Miyazaki, K. Satake, Y. Fujii, H. Miyake, S. Sakai, Y. Yamanaka, *et al.* (2011). A unified

source model for the 2011 Tohoku earthquake, *Earth Planet. Sci. Lett.* **310,** 480–487.

Kurahashi, S., and K. Irikura (2013). Short-period source model of the 2011 M_w 9.0 Off the Pacific Coast of Tohoku earthquake, *Bull. Seismol. Soc. Am.* **103,** 1373–1393, doi: 10.1785/0120120157.

Lorito, S., F. Romano, S. Atzori, X. Tong, A. Avallone, J. McCloskey, M. Cocco, E. Boschi, and A. Piatanesi (2011). Limited overlap between the seismic gap and coseismic slip of the great 2010 Chile earthquake, *Nature Geosci.* **4,** 173–177.

McNeill, A. F., M. G. Bostock, G. C. Rogers, and J. C. Shragge (2004). The effect of forearc mantle serpentinization on ground motions from megathrust and intraslab events in the Cascadia subduction zone, *Bull. Seismol. Soc. Am.* **94,** 147–154.

Murotani, S., H. Miyake, and K. Koketsu (2008). Scaling of characterized slip models for plate-boundary earthquakes, *Earth Planets Space* **60,** 987–991.

Murotani, S., K. Satake, and Y. Fujii (2013). Scaling relations of seismic moment, rupture area, average slip, and asperity size for M ~ 9 subduction-zone earthquakes, *Geophys. Res. Lett.* **40,** 5070–5074, doi: 10.1002/grl.50976.

Ocola, L. C., J. Luetgert, L. T. Aldrich, R. P. Meyer, and C. E. Helsey (1995). Velocity structure of the coastal region of southern Peru from seismic refraction/wide-angle reflection data, *J. Geodyn.* **20,** 1–30.

Petersen, M. D., C. H. Cramer, and A. D. Frankel (2002). Simulations of seismic hazard for the Pacific Northwest of the United States from earthquakes associated with the Cascadia subduction zone, *Pure Appl. Geophys.* **159,** 2147–2168.

Petersen, M. D., A. Frankel, S. Harmsen, C. Mueller, K. Haller, R. Wheeler, R. Wesson, Y. Zeng, O. Boyd, D. Perkins, *et al.* (2008). Documentation for the 2008 updated of the United States National Seismic Hazard Maps, *U.S. Geol. Surv. Open-File Rept. 2008-1128*, 61 pp.

Pitarka, A., H. K. Thio, P. Somerville, and L. F. Bonilla (2013). Broadband ground-motion simulation of an intraslab earthquake and nonlinear site response: 2010 Ferndale, California, earthquake case study, *Seismol. Res. Lett.* **84,** 785–795.

Satake, K., Y. Fujii, T. Harada, and Y. Namegaya (2013). Tsunami source model of the 2011 Tohoku earthquake and comparison with the 1896 Sanriku and 869 Jogan earthquakes, *Geophys. Res. Abstr.* **15,** EGU2013-4222-1, EGU General Assembly.

Skarlatoudis, A. A., and C. B. Papazachos (2012). Preliminary study of ground motions of Tohoku, Japan earthquake of 11 March 2011: Assessing the influence of anelastic attenuation and rupture directivity, *Seismol. Res. Lett.* **83,** 119–129.

Somerville, P. (1993). Engineering applications of strong ground motion simulation, *Tectonophysics* **218,** 195–219.

Somerville, P., R. Graves, and N. Collins (2008). Ground motions from large Cascadia subduction earthquakes, *U.S. Geol. Surv. Final Rept. Award Number 06HQGR0160*.

Somerville, P., K. Irikura, R. Graves, S. Sawada, D. Wald, N. Abrahamson, Y. Iwasaki, T. Kagawa, N. Smith, and A. Kowada (1999). Characterizing earthquake slip models for the prediction of strong ground motion, *Seismol. Res. Lett.* **70,** 59–80.

Somerville, P., T. Sato, T. Ishii, N. F. Collins, K. Dan, and H. Fujiwara (2002). Characterizing heterogeneous slip models for large subduction earthquakes for strong ground motion prediction, *11th Japan Earthquake Engineering Symposium*, Tokyo, Japan, 20–22 November 2002.

Somerville, P., M. K. Sen, and B. P. Cohee (1991). Simulation of strong ground motions recorded during the 1985 Michoacan, Mexico and Valparaiso, Chile earthquakes, *Bull. Seismol. Soc. Am.* **81,** 1–27.

Somerville, P., A. Skarlatoudis, and W. Li (2013a). Ground motions and tsunamis from M_w 9.0 Cascadia subduction earthquakes based on validations using the M_w 8.8 Maule, Chile earthquake of 2010, *U.S. Geol. Surv. Final. Rept.*, 74 pp.

Somerville, P., A. Skarlatoudis, and W. Li (2013b). Ground motions and tsunamis from large Cascadia subduction earthquakes based on the 2011 Tokoku, Japan earthquake, *U.S. Geol. Surv. Final. Rept.*, 81 pp.

Somerville, P., H. K. Thio, G. Ichinose, N. Collins, A. Pitarka, and R. Graves (2003). Earthquake source and ground motion characteristics of the June 23, 2001 M_w 8.4 Arequipa, Peru, earthquake, abstract, *Seismol. Res. Lett.* **74,** 223.

Stewart, J. P., S. Midorikawa, R. W. Graves, K. Khodaverdi, H. Miura, Y. Bozorgnia, and K. W. Campbell (2013). Implications of M_w 9.0 Tohoku-oki Japan earthquake for ground motion scaling with source, path, and site parameters, *Earthq. Spectra* **29,** S1–S21.

Wald, D. J., and P. G. Somerville (1995). Variable slip rupture model of the great 1923 Kanto, Japan earthquake: Geodetic and body-waveform analysis, *Bull. Seismol. Soc. Am.* **85,** 159–177.

Wessel, P., and W. H. F. Smith (1998). New, improved version of the Generic Mapping Tools released, *Eos Trans. AGU* **79,** 579.

Yokota, Y., K. Koketsu, Y. Fujii, K. Satake, S. Sakai, M. Shinohara, and T. Kanazawa (2011). Joint inversion of strong motion, teleseismic, geodetic, and tsunami datasets for the rupture process of the 2011 Tohoku earthquake, *Geophys. Res. Lett.* **38,** doi: 10.1029/2011GL050098.

Yoshida, K., K. Miyakoshi, and K. Irikura (2011). Source process of the 2011 Off the Pacific Coast of Tohoku earthquake inferred from waveform inversion with long-period strong-motion records, *Earth Planets Space* **63,** 577–582.

Yue, H., and T. Lay (2011). Inversion of high-rate (1 sps) GPS data for rupture process of the 11 March 2011 Tohoku earthquake (M_w 9.1), *Geophys. Res. Lett.* **38,** doi: 10.1029/2011GL048700.

Zhao, J. X., J. Zhang, A. Asano, Y. Ohno, T. Oouchi, T. Takahashi, H. Ogawa, K. Irikura, H. K. Thio, P. G. Somerville, *et al.* (2006). Attenuation relations of strong motion in Japan using site classification based on predominant period, *Bull. Seismol. Soc. Am.* **96,** 898–913.

AECOM
915 Wilshire Boulevard
Los Angeles, California 90017
andreas.skarlatoudis@aecom.com
paul.somerville@aecom.com
hong.kie.thio@aecom.com
jeff.bayless@aecom.com

Manuscript received 17 September 2015